Multi-tool optimization for computer controlled optical surfacing

XIAOLONG KE,[1] TIANYI WANG,[2,*] ZILI ZHANG,[3] LEI HUANG,[2] CHUNJIN WANG,[3] VIPENDER S. NEGI,[4,5] WESLIN C. PULLEN,[6] HEEJOO CHOI,[6,7] DAEWOOK KIM,[6,7,8] AND MOURAD IDIR[2]

[1] *School of Mechanical and Automotive Engineering, Xiamen University of Technology, Xiamen 361024, China*
[2] *National Synchrotron Light Source II (NSLS-II), Brookhaven National Laboratory, PO Box 5000, Upton, NY 11973, USA*
[3] *State Key Laboratory of Ultra-precision Machining Technology, Department of Industrial and Systems Engineering, The Hong Kong Polytechnic University, Hung Hom, Kowloon, Hong Kong, China*
[4] *Council of Scientific and Industrial Research-Central Scientific Instruments Organisation (CSIR-CSIO), Chandigarh 160030, India*
[5] *Academy of Scientific and Innovative Research (AcSIR), Ghaziabad 201002, India*
[6] *James C. Wyant College of Optical Sciences, the University of Arizona, 1630 E. University Blvd., P.O. Box 210094, Tucson, AZ 85721-0094, USA*
[7] *Large Binocular Telescope Observatory, Univ. of Arizona, Tucson, AZ 85721, USA*
[8] *Department of Astronomy and Steward Observatory, Univ. of Arizona, 933 N. Cherry Ave., Tucson, AZ 85721, USA*
[*] *tianyi@bnl.gov*

Abstract: With the rapid development of precision technologies, the demand of high-precision optical surfaces has drastically increased. These optical surfaces are mainly fabricated with computer controlled optical surfacing (CCOS). In a CCOS process, a target surface removal profile is achieved by scheduling the dwell time for a set of machine tools. The optimized dwell time should be positive and smooth to ensure convergence to the target while considering CNC dynamics. The total run time of each machine tool is also expected to be balanced to improve the overall processing efficiency. In the past few decades, dwell time optimization for a single machine tool has been extensively developed. While the methods are applicable to multi-tool scenarios, they fail to consider the overall contributions of multiple tools simultaneously. In this paper, we conduct a systematic study on the strategies for multi-tool dwell time optimization and propose an innovative method for simultaneously scheduling dwell time for multiple tools for the first time. First, the influential factors to the positiveness and smoothness of dwell time solutions for a single machine tool are analyzed. The compensation strategies that minimize the residual while considering the CNC dynamics limit are then proposed. Afterwards, these strategies are extended to the proposed multi-tool optimization that further balances the run time of machine tools. Finally, the superiority of each strategy is carefully studied via simulation and experiment. The experiment is performed by bonnet polishing a 60 mm × 60 mm mirror with three tools of different diameters (*i.e.,* 12 mm, 8 mm, and 5 mm). The figure error of the mirror is reduced from 45.42 nm to 11.18 nm root mean square in 13.28 min. Moreover, the measured polishing result well coincides with the estimation, which proves the effectiveness of the proposed method.

1. Introduction

Over the past few decades, the need for ultra-precision optical components has been increasing both in industry and consumer applications, such as telescopes for space exploration [1,2], reflective mirrors for synchrotron radiation and free-electron laser facilities [3,4], and high-NA

optics in EUV lithography [5]. The surface form deviation requirements range from microns for visible light applications down to sub-nanometer levels for X-ray imaging at the diffraction limit. Typically, these optical components are produced by precision grinding followed by sub-aperture Computer Controlled Optical Surfacing (CCOS) where the contact area between machine tool and workpiece is much smaller than the Clear Aperture (CA) of the workpiece. Since it was first proposed in 1977 [6], a series of CCOS techniques have been developed, such as bonnet polishing [7], fluid jet polishing [8], magnetorheological finishing [9], ion beam figuring [10], *etc*. Different CCOS processes are adopted based on the requirement of the precision and shapes of the desired optical surfaces. A sophisticated CCOS system is usually equipped with a set of machine tools with different sizes and shapes to correct surface errors with different spatial frequencies. These tools are deterministically guided by predetermined dwell time at successive dwell points on tool paths to remove material from optical surfaces. To alleviate the frequent acceleration and deceleration of the CNC units, the discrete dwell time is always converted to continuously varying feedrates [11,12] in real implementation. Therefore, a reliable dwell time solution is fundamental.

A desired dwell time solution should be positive and smooth, and need to consider CNC dynamics limits. Single-tool based optimization methods have been extensively studied and advanced in the literature. The iterative Van Cittert algorithm [13] was first introduced to CCOS in 1977 [6], which iteratively corrects dwell time values based on the smoothness assumption that dwell time should be proportional to the target surface removal profile. However, this method may fail to converge if a Tool Influence Function (TIF) (*i.e.,* machine tool footprint) is not axially-symmetric or does not have a central peak [6]. To improve the convergence, a self-adaptive coefficient based on the volumetric removal rate of a TIF was introduced to stabilize the iterative process [14]. Since the Van Cittert algorithm converges to an inverse filter when noise is absent [15], a thresholded inverse filtering algorithm based on Fourier transform [16] was proposed. However, the selection of a proper threshold that eliminates the negative dwell time areas was nontrivial until the more advanced Robust Iterative Fourier Transform-based Algorithm (RIFTA) [17] and Robust Iterative Surface Extension (RISE) [18] were proposed. Based on Bayesian interference, the Richard-Lucy deconvolution [19,20] was introduced to CCOS for dwell time optimization. The employed multiplicative algorithm ensured the non-negativeness of dwell time if the initial guess is non-negative [21]. All the methods mentioned so far assumed that surface sampling points are on a regular grid which can hardly be applied to aspherical or even free-form optics fabrication. Also, they did not consider the polishing paths. It is usually time-consuming and error-prone to re-adapt the calculated dwell time to their nearest dwell points along the actual tool path.

To alleviate this problem, the matrix-based method was proposed that transformed the convolutional material removal model into finding the optimal solution of a linear, ill-posed inverse problem [22]. This method has no restrictions on tool paths and surface shapes, however, it has not been favored because of the time-consuming construction of the design matrix for large workpiece until the recent advancement of higher-performance computing technologies. In addition, the mathematically optimal solution is usually not directly applicable to actual manufacturing processes because of the resulted negative and unsmooth entries in the dwell time. Thus, either the Tikhonov regularization [11,22–25] with a damping factor or the other constraints [26–30] were introduced to balance the fluctuation in dwell time and the residual error. For the former case, since the design matrix is always large but sparse, an efficient iterative Least Squares with QR (LSQR) factorization solver [31] was used. The selection of a proper damping factor was based on trial-and-error [22,23] or the "L" curve obtained by time-consuming line search [11]. A typical range for the damping factor numerically studied from the peak removal rate of a TIF was then proposed. However, this range was not always stable to obtain positive and smooth solutions. For the latter case, different constraints on the positiveness [27], residual error

[26], dwell time gradient [26,28], and CNC dynamic limits [27,30] were added to the model and a Constrained Linear Least Squares (CLLS) solver was applied to solve the systems. However, the introduction of these constraints made the solution process too computationally expensive to be applied in practice. Recently, a Universal Dwell time Optimization (UDO) that combined the merits of arbitrary dwell points of the matrix-based method and the smoothness assumption of the iterative method was proposed [10], and an analytical feedrate scheduling method [32,33] was proposed that could even optimize feedrates and tool paths simultaneously from a well-defined analytical material removal equation, pushing the single-tool optimization to a new era of high accuracy and robustness.

While the single-tool optimization methods are directly applicable to multi-tool scenarios, they can only take one machine tool into account at a time, lacking the capability to balance the run time across all the tools in a CCOS system, which is critical to improve the overall manufacturing efficiency. Although the machine tools are usually used sequentially in a polishing cycle, the planning of them can be performed non-sequentially. Thus, based on the matrix-based method, a non-sequential, multi-tool optimization was proposed to calculate dwell time for a set of machine tools simultaneously [34]. This method balanced the run time of each tool and reduced the Middle-Spatial-Frequency (MSF) errors in the residual. However, the gradient-based search might fail to converge to an optimal solution, and the employed Non-Negative Least Squares (NNLS) algorithm brought large fluctuations into dwell time solutions.

In this paper, to fill the gap between single-tool and multi-tool optimizations, we conduct a systematic study on the necessary strategies for multi-tool optimization in CCOS. Firstly, the influential factors of positiveness and smoothness, namely the number of iterations and the damping factor, in matrix-based, single-tool dwell time optimization are analyzed. Secondly, an automatic damping factor selection strategy for the Tikhonov regularization based on CNC dynamics are provided to ensure positive dwell time solutions. For the smoothness requirement, surface extension of the CA before optimization is necessary, yet the total surfacing time will be longer. Thirdly, the single-tool strategies are extended to multi-tool optimization method by further considering the balance of the run time of each machine tool. Also, it is found that the smoothness is automatically guaranteed in the proposed method so that surface extension is not necessary thus the total run time is reduced. Finally, the performance of the single-tool and the proposed methods applied in multi-tool scheduling are studied via simulation, and a polishing experiment of a 60 mm × 60 mm CA HK9L flat is performed using three bonnet tools with different sizes (*i.e.,* with diameters of 12 mm, 8 mm, and 5 mm). The estimated residual from the proposed method is 6.9 nm Root Mean Square (RMS). The measured residual after polishing with the three tools is 11.2 nm RMS, which is so close to and duplicates the shape of the estimation that the effectiveness of the proposed strategy is verified.

The rest of the paper is organized as follows. Section 2 introduces the material removal model for dwell time optimization, followed by the study and analysis of the matrix-based, single-tool optimization in Section 3. Section 4 demonstrates the proposed multi-tool optimization, highlighting its superiority over the conventional methods. A real experiment based on the proposed method is then presented in Section 5 to verify the proposed method. Section 6 discusses the limitation and possible extension of the proposed method, and Section 7 concludes the paper.

2. Material removal model

In this section, the deviation of the matrix-based convolutional polishing model [12] is described. Afterwards, the dwell time optimization based on the Tikhonov regularized linear system and the corresponding iterative Least-Squares with MR (LSMR) factorization solver [35] are introduced. It is worth mentioning that the study conducted in this paper is based on LSMR instead of LSQR because it converges faster for incompatible linear systems (*i.e.,* the dwell points are less than the

sampling points of a measured workpiece surface) and is more computationally efficient than CLLS when applied to multi-tool optimization.

The general partial differential equation [12] that governs material removal in CCOS can be expressed as

$$\frac{\partial z(\mathbf{r})}{\partial t} = -b(\mathbf{r} - \mathbf{P}), \tag{1}$$

where z is the evolving height in the CA, t is the dwell time with $0 \leq t \leq T$ where T is the total dwell time in one process, $\mathbf{r}$ defines the surface of the workpiece, $\mathbf{P} = (\xi, \eta)$ is the dwell point of the machine tool on the workpiece, and b is the TIF. Integrating both sides of Eq. (1), the material removed over the CA is obtained as

$$z(\mathbf{r}) = \int_0^T -b(\mathbf{r} - \mathbf{P}) \, dt. \tag{2}$$

For numerical computation, Eq. (2) is discretized by considering the tool path points as

$$z(\mathbf{r}_n) = \sum_{m=1}^{M} -b(\mathbf{r}_n - \mathbf{P}_m) t_m, \tag{3}$$

for $n = 1, 2, \ldots, N$ where N is the total number of elements in $z(\mathbf{r}_n)$, M is the number of dwell points on a tool path, and t_m is the dwell time at the dwell point $\mathbf{P}_m$. Equation (3) can be expressed in a matrix form as

$$\underbrace{\begin{pmatrix} b_{1,1} & b_{1,2} & \ldots & b_{1,M} \\ b_{2,1} & b_{2,2} & \ldots & b_{2,M} \\ \vdots & \vdots & \ddots & \vdots \\ b_{N,1} & b_{N,2} & \ldots & b_{N,M} \end{pmatrix}}_{\mathbf{B}} \underbrace{\begin{pmatrix} t_1 \\ t_2 \\ \vdots \\ t_M \end{pmatrix}}_{\mathbf{t}} = \underbrace{\begin{pmatrix} z_1 \\ z_2 \\ \vdots \\ z_N \end{pmatrix}}_{\mathbf{z}}, \tag{4}$$

where $z_n = z(\mathbf{r}_n)$ and $b_{n,m} = b(\mathbf{r}_n - \mathbf{P}_m)$. Therefore, by substituting $\mathbf{z}$ with the target removal profile $\mathbf{z}_d$, $\mathbf{t}$ can be obtained by solving the linear system in Eq. (4).

The number of solutions of Eq. (4) depends the numbers of M and N. Since current optical metrology techniques (such as interferometry) are often equipped with dense CCD arrays, we have $M<N$, namely the number of dwell points on a tool path is less than the number of sampling points of a measured workpiece map [24], where Eq. (4) is an incompatible linear system. In addition, the matrix $\mathbf{B}$ is constructed by overlapping a TIF across different dwell points on the workpiece, its columns are nearly linearly dependent so that Eq. (4) is so ill-posed that it is nontrivial to obtain a reasonable solution. A small perturbation in either $\mathbf{B}$ or $\mathbf{z}$ may significantly influence the results, and the solution becomes non-robust against practical errors and noise.

To solve the ill-posed Eq. (4), the Tikhonov regularization is adopted in this study as

$$\begin{pmatrix} \mathbf{B} \\ \lambda \mathbf{I} \end{pmatrix} \mathbf{t} = \begin{pmatrix} \mathbf{z}_d \\ \mathbf{0} \end{pmatrix}, \tag{5}$$

in which the matrix $\mathbf{B}$ is extended by an $M \times M$ diagonal matrix, where the damping factor λ on its diagonal is introduced to damp the influence of the small perturbations in $\mathbf{B}$ or $\mathbf{z}_d$ and stabilize the solution space.

It is obvious that $\mathbf{B}$ is a large but sparse matrix, where the non-zero entries concentrate on its diagonals. One efficient solver to solve large and sparse linear systems is LSQR [31], which implements an iterative conjugate-gradients method based on the Golub-Kahan bidiagonlization.

LSQR monotonically reduces the l_2 norm of the residual error, *i.e.,* $|\mathbf{z}_d - \mathbf{z}| = |\mathbf{z}_d - \mathbf{Bt}|$, which is desirable on compatible systems. However, as mentioned above, Eq. (5) is always incompatible in CCOS. Therefore, as suggested in [35], a more efficient LSMR algorithm instead of LSQR is preferred since it reduces both $|\mathbf{z}_d - \mathbf{Bt}|$ and $\left|\mathbf{B}^{\mathrm{T}}\left(\mathbf{z}_d - \mathbf{Bt}\right)\right|$ monotonically so that it may converge significantly sooner than LSQR if looser stopping tolerances and an approximate solution are acceptable. As will be demonstrated below, LSMR is robust and reliable in obtaining a proper solution to both single-tool and multi-tool dwell time solutions if the stopping tolerances and the damping factor are wisely selected.

For the studies that will be conducted in Sections 3 and 4, the data shown in Fig. 1 will be used. Figure 1(a) shows the target removal in a 200 mm × 200 mm CA that measured from a silicon surface. The three Gaussian TIFs with Full Width at Half Maximum (FWHM) of 24 mm, 16 mm and 6 mm, respectively, are given in Fig. 1(b). The raster tool paths, as shown in Fig. 1(c), are used for all the three tools, and the range of each tool path is larger than the outline perimeter of the CA by the radius of the corresponding TIF. The respective machining intervals are set as 10.5 mm, 7.0 mm, and 2.8 mm.
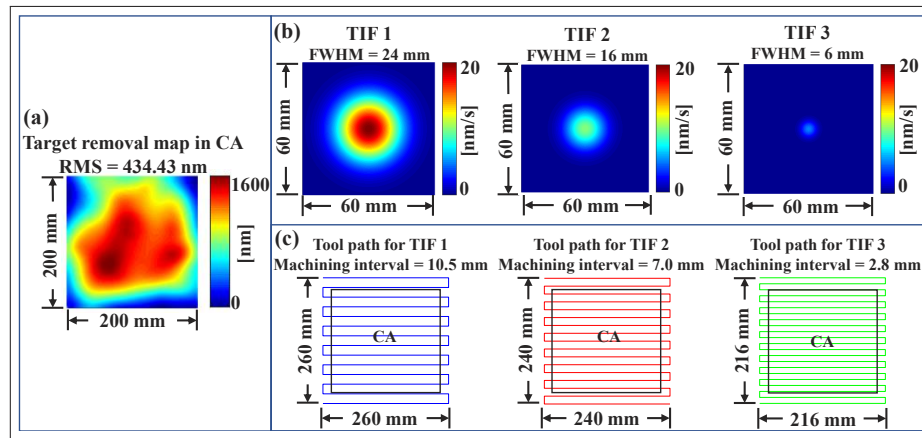

Fig. 1. The target removal map (a), three TIFs (b) and raster tool paths (c) used in the simulation.

Three criteria are used to evaluate the dwell time optimization, namely the estimated residual in the CA, the positiveness, and the smoothness of the dwell time. Firstly, the estimated residual is the indicator of convergence. In real applications, this value should be minimized by the dwell time optimization according to a certain TIF's removal capability. Secondly, the dwell time solution used to achieve the minimized residual in the CA should be positive, since CCOS processes are only capable of removing materials, and any CNC unit cannot implement zero dwell time (or infinite feedrates). Finally, the dwell time solution is expected to be spatially-and-temporally smooth, since frequent acceleration or deceleration will incur vibrations to the machine tool and thus reduce the convergence to the expected residual.

3. Analysis on the single-tool dwell time optimization

In this section, the performance of applying LSMR to single-tool dwell time optimization is studied. In LSMR, two key parameters, namely the number of iterations and the damping factor, λ, have effects on the residual in the CA, as well as the positiveness and smoothness of the dwell time. These effects are first evaluated in the simulation, after which the compensation strategies and an automatic parameter optimization for LSMR are proposed.

3.1. Evaluation of the key parameters in LSMR

Mathematically, the optimal solution to Eq. (4) is the one that minimizes $\frac{1}{2}\,|\mathbf{z_d} - \mathbf{Bt}|$, and the Moore-Penrose Pseudo INVerse (PINV) can be used to directly obtain this solution. The dwell time for TIF 1 shown in Fig. 1(b) that is calculated by PINV is given in Fig. 2(a). The corresponding estimated residual in the CA is shown in Fig. 2(c), which is the smallest residual that TIF 1 can theoretically achieve. However, this dwell time solution can hardly be implemented in practice, since many entries are negative, and the variation of the dwell time between two consecutive dwell points (see Fig. 2(b)) is so large that this is unachievable by any CNC unit.
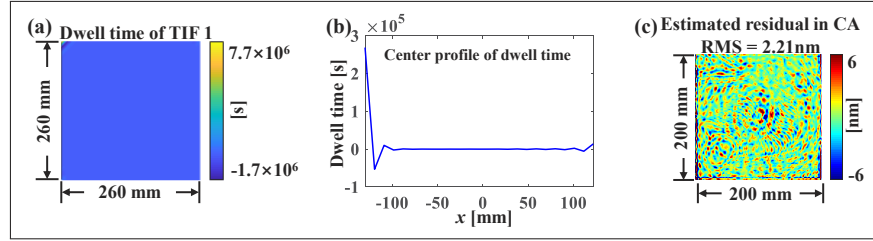

Fig. 2. Dwell time for TIF 1 (a), its center profile along the *x* direction (b), and the estimated residual in the CA (c) calculated using the Moore–Penrose pseudo inverse.

In LSMR, the maximum number of iterations (i_{max}) and λ have great influences on the smoothness and positiveness of the dwell time solution. Ultimately, LSMR converges to the PINV's result in Fig. 2 if it would be run for $i_{max} = +\infty$ and $\lambda = 0$. However, to maintain the positiveness and smoothness of the dwell time while keeping a low residual, it is essential to choose the appropriate values for these two parameters. Therefore, the negative dwell time ratio, the smoothness of the dwell time and the residual RMS values in the CA with respect to different i_{max}'s and λ's are studied in Fig. 3.
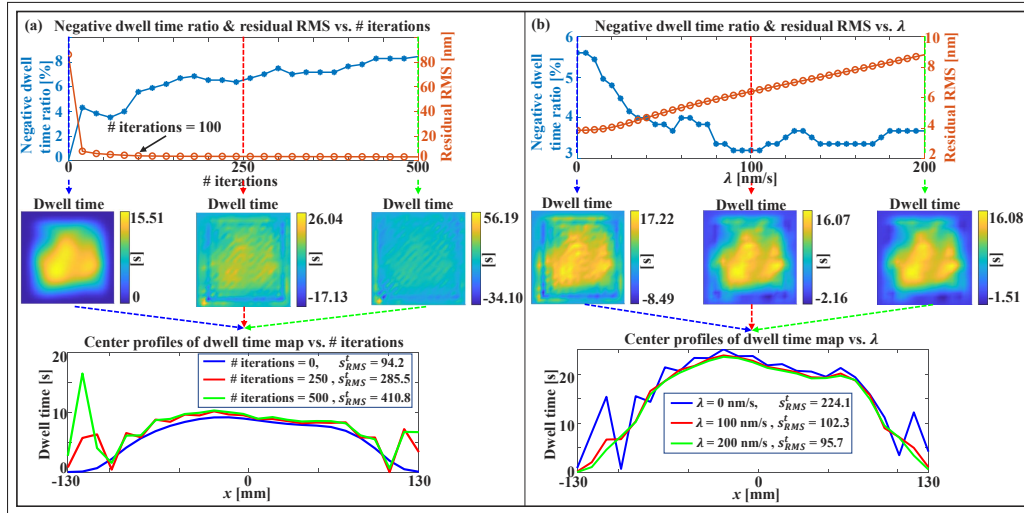

Fig. 3. The negative dwell time ratio and residual RMS versus the numbers of iterations (a) and the values of λ (b) in the LSMR algorithm.

Figure 3(a) shows the influence caused by i_{max} from 0 to 500 with $\lambda = 0$ nm/s fixed. This is achieved by removing all of the stopping criteria in LSMR except the maximum number of

iterations. With the increase of iterations, the negative dwell time ratio increases, and the residual RMS rapidly decreases before $i_{max} = 100$, but the variations after that are tiny. To quantitatively evaluate the smoothness of the dwell time, the slope RMS magnitude of the center profile of a dwell time map along the x direction is calculated as

$$s_{RMS}^t = \text{RMS} \left[\frac{t_{i+1} - t_i}{x_{i+1} - x_i} \right], \tag{6}$$

for $i = 1, 2, \ldots, P$ where P is the number of dwell points in the x direction. The center profiles along the x direction of the dwell time maps at $i_{max} = 0, 250,$ and 500 are plotted, from which it is found that the dwell time becomes less smooth as i_{max} gets larger. From these analyses, we can conclude that, as i_{max} increases, the residual keeps decreasing, however, both the positiveness and smoothness of the dwell time become worse (*i.e.,* high-gradient dwell time solution).

A similar process is performed with respect to varying λ's from 0 nm to 200 nm with $i_{max} = 100$ fixed. As shown in Fig. 3(b), with λ increased, the residual RMS grows almost linearly. On the other hand, however, the dwell time becomes considerably smoother, and the negative dwell time ratio decreases.

In a word, as i_{max} decreases or λ increases, the dwell time becomes smoother and more positive, but the residual RMS is larger. Thus, it is crucial to find the appropriate trade-off between the smoothness and positiveness of dwell time, and the residual RMS to achieve the optimal dwell time solution. The strategies used to achieve this balance for single-tool dwell time optimization are detailed as follows.

3.2. Single-tool optimization study

The first attempt is to determine the appropriate λ and i_{max} for the LSMR algorithm. In the literature, these two parameters have been selected by trial-and-error [22–24], which is inconvenient and makes it hard to achieve the lowest possible residual RMS. Thus, as shown in Algorithm 1, we propose an automatic Single-Tool Optimization (STO) algorithm, which automates the parameter-tuning in LSMR by minimizing the residual RMS while considering the maximum feedrate limit of the CNC unit and maintaining the positiveness of the dwell time.

3.2.1. Automatic damping factor (λ) optimization

As shown in Eq. (5), λ is a hyper-parameter in LSMR. Although the previous research works either attempted to constrain the search range [23] or found typical values of λ [24], the methods did not consider the positiveness requirement of **t**. Therefore, we propose an automatic λ optimization algorithm using the merit function given in Lines 13 - 17 in Algorithm 1.

In the merit function, **t** is based on the current λ and adjusted to be positive (Lines 20 - 21). The positiveness is achieved by offsetting the dwell time by the minimum dwell time, τ, that is calculated with the maximum feedrate, v_{max}, of the CNC unit, and the minimum machining intervals on the tool path, $\Delta \mathbf{x}$, as shown in Line 2. To evaluate the performance of the current **t**, the RMS of the residual is calculated in Lines 15 and 16.

It is obvious that the derivatives of the merit function can hardly be calculated, thus a derivative-free optimization is considered an appropriate option. In this study, since λ is the only parameter to optimize, the well-known pattern search algorithm is selected (Lines 6 - 8) due to its simplicity and computational efficiency [36]. It is worth noting that, to allow the pattern search algorithm to converge faster, a good initial guess, λ_0, is necessary. Although λ_0 can be selected as a typical value suggested in [24], we found that it is not suitable for the positiveness adjustment. Therefore, as shown in Lines 3 - 5, another more flexible derivative-free optimization method, the Particle Swarm Optimization (PSO), is used to generate a good λ_0 because it does not require

an initial guess. To improve the computational efficiency, PSO is stopped early when it stalls at a merit function value. Finally, **t** is calculated using the optimized damping factor, λ_{opt} in Line 9.

Algorithm 1: Single-tool optimization (Eq. 5)

1 **Function** STO (**B**, $\mathbf{z}_d$, ϵ, v_{max}, $\Delta\mathbf{x}$, $i_{max} = 100$):
2    $\tau \leftarrow \dfrac{\Delta\mathbf{x}}{v_{max}}$
3    $\lambda_0 \leftarrow$ ParticleSwarm (@MeritSTO,
4   **B**, $\mathbf{z}_d$, τ, ϵ, i_{max}
5   )
6    $\lambda_{opt} \leftarrow$ PatternSearch (@MeritSTO, λ_0,
7   **B**, $\mathbf{z}_d$, τ, ϵ, i_{max}
8   )
9   **t** $\leftarrow$ CalcTime (**B**, $\mathbf{z}_d$, τ, λ_{opt}, ϵ, i_{max})
10   **return t**
11 **End Function**
12
13 **Function** MeritSTO (λ, **B**, $\mathbf{z}_d$, τ, ϵ, i_{max}):
14   **t** $\leftarrow$ CalcTime (**B**, $\mathbf{z}_d$, τ, λ, ϵ, i_{max})
15   $\mathbf{z}_r = \mathbf{z}_d - \mathbf{Bt}$
16   **return** RMS ($\mathbf{z}_r$)
17 **End Function**
18
19 **Function** CalcTime (**B**, $\mathbf{z}_d$, τ, λ, ϵ, i_{max}):
20   **t** $\leftarrow$ LSMR (**B**, $\mathbf{z}_d$, λ, ϵ, i_{max})
21   **t** $\leftarrow$ **t**$-$MIN (**t**) $+ \tau$
22 **End Function**

Algorithm 2: Multi-tool optimization (Eq. 8)

1 **Function** MTO (**B**, $\mathbf{z}_d$, ϵ, v_{max}, $\Delta\mathbf{x}$, $i_{max} = 100$):
2    $\tau_1, \tau_2, ..., \tau_K \leftarrow \dfrac{\Delta\mathbf{x_1}}{v_{max}}, \dfrac{\Delta\mathbf{x_2}}{v_{max}}, ..., \dfrac{\Delta\mathbf{x_K}}{v_{max}}$
3    $\lambda_0 \leftarrow$ ParticleSwarm (@MeritMTO,
4   **B**, $\mathbf{z}_d$, τ, ϵ, i_{max}
5   )
6    $\lambda_{opt} \leftarrow$ PatternSearch (@MeritMTO, λ_0,
7   **B**, $\mathbf{z}_d$, τ, ϵ, i_{max}
8   )
9   **t** $\leftarrow$ CalcTime (**B**, $\mathbf{z}_d$, λ_{opt}, ϵ, i_{max})
10   **return t**
11 **End Function**
12
13 **Function** MeritMTO (λ, **B**, $\mathbf{z}_d$, τ, ϵ, i_{max}):
14   **t** $\leftarrow$ CalcTime (**B**, $\mathbf{z}_d$, τ, λ, ϵ, i_{max})
15   $\mathbf{z}_r = \mathbf{z}_d - \mathbf{Bt}$
16   **return** RMS ($\mathbf{z}_r$)
17 **End Function**
18
19 **Function** CalcTime (**B**, $\mathbf{z}_d$, τ, λ, ϵ, i_{max}):
20   **t** $\leftarrow$ LSMR (**B**, $\mathbf{z}_d$, λ, ϵ, i_{max})
21   $p \leftarrow 0$
22   **for** $i \leftarrow 1$ **to** K **do**
23     $q = p + 1$
24     $q =$ Length (τ_i) $+ q$
25     $\mathbf{t}_i = \mathbf{t}[p : q]$
26     $\mathbf{t}[p : q] \leftarrow \mathbf{t}_i - $MIN ($\mathbf{t}_i$) $+ \tau_i$
27   **end**
28 **End Function**

3.2.2. Fine tuning of the stopping criteria for LSMR

As suggested by Fig. 3(a), the variation of the residual RMS is tiny when $i_{max}>100$. Therefore, in this study, as shown in Line 1 in Algorithm 1, the maximum number of iterations of LSMR

is fixed at $i_{max} = 100$. In addition, to further improve the computational efficiency, a precision tolerance, ϵ, is introduced to stop the LSMR's iterations early in Lines 9 and 14 in Algorithm 1. In this study, $\epsilon = 1 \times 10^{-3}$ nm is used, meaning that the iteration will stop when the RMS difference between the two adjacent merit function evaluations is less than 1×10^{-3} nm.

3.2.3. Smoother dwell time solution with surface extension

Through the above analysis, STO can wisely adjust i_{max} and λ to reach low residual RMS and ensure the positiveness of **t**. Figure 4(a) shows the **t** and estimated residual in the CA calculated by STO with $v_{max} = 50$ mm/s for TIF 1. It is found that **t** is positive (*i.e.,* **t** ≥ 0.21 s) and the achieved residual RMS (*i.e.,* 4.89 nm) is comparable to the lowest point in Fig. 3(b). However, as shown in Fig. 4(c), the dwell time profile along the x direction is still not smooth enough, since STO does not include the smoothness constraint in the optimization.
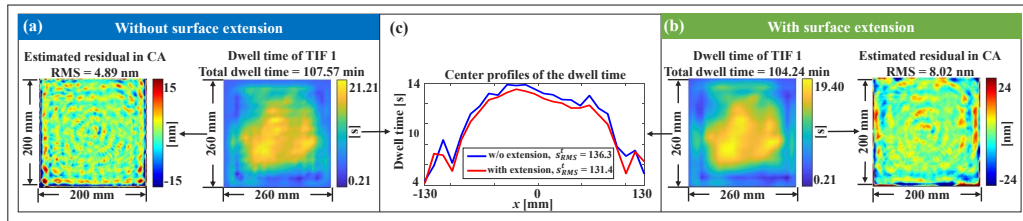

Fig. 4. Comparison between the dwell time optimization without surface extension (a) and with surface extension (b). The center profiles of the dwell time maps (c) indicate that the dwell time solution with surface extension is smoother and thus preferred.

To further improve the smoothness of **t**, as suggested in the previous research works [10,24,37], surface extension can be used to extend the calculation range from the CA to the entire dwell area under the tool path. Although tools in contact-based CCOS systems have overhang issues at the edges of a workpiece, surface extension is still necessary in the optimization for the smoothness of the dwell time [37]. However, the dwell time solution is still confined in the area allowing the actual runs. Therefore, as shown in Fig. 4(b), surface extension is performed before applying STO. As shown in Fig. 4(c), **t** obtained with the extension is much smoother than that calculated using the CA only. It is worth mentioning that, however, the residual RMS as shown in 4(b) is not effectively controlled after surface extension. This is mainly because the extension algorithm is greatly affected by the existing shape of the target removal map, and the continuity along the extension boundary is hard to guarantee. If a lower residual RMS is expected, the more complex iterative surface extension [18] should be used, which is not considered in this study.

In summary, according to the results in this section, the single-tool optimization strategy is to combine the surface extension with the STO algorithm to achieve a positive and smooth dwell time solution that minimizes the residual in the CA.

4. Multi-tool optimization

A sophisticated CCOS system is usually equipped with multiple machine tools with different types, shapes and sizes, which enable the effective and efficient correction of surface errors with different spatial frequencies. For example, a Zeeko IRP200 CCOS machine is equipped with both a bonnet tool and a Fluid Jet Polishing (FJP) head. In the coarse polishing phase, TIFs with different sizes can be easily generate by either adjusting the pressure of one bonnet tool or directly changing the bonnet head. The fine finish of the workpiece can then be carried out by the small TIF of FJP.

Although the STO strategies proposed in Section 3 are directly applicable to the multi-tool scenario by sequentially optimizing the dwell time for the TIFs, it fails to consider the overall

contribution of multiple tools simultaneously. This is manifested in Fig. 5(a), where the dwell time maps for the three TIFs shown in Fig. 1 are sequentially optimized with STO, in which the residual estimated from the current TIF serves as the target removal for the next smaller TIF. With STO, although a final estimated residual of 0.71 nm is achieved, the total dwell time (*i.e.,* 96.58 min, 284.97 min, and 2412.78 min, respectively) of the three tools is not balanced. Also, as shown in Fig. 5(c), the dwell time profile along the feed direction is not smooth, which restricts the practical use of these solutions.
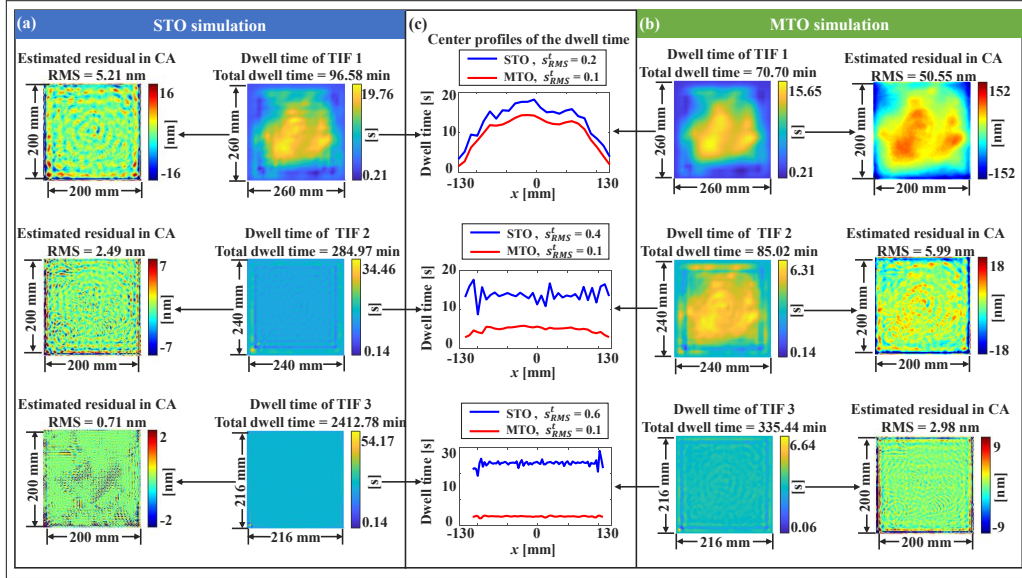

Fig. 5. Comparison between the STO (a) and the MTO (b) optimized dwell time for the three TIFs. The center profiles of the dwell time maps (c) and the total dwell time indicate that MTO achieves smoother and more balanced dwell time solutions for multiple TIFs.

The previous research work has verified that, even though the actual polishing runs are usually scheduled for the TIFs with the sizes from big to small sequentially, the dwell time optimization can be performed non-sequentially for all the TIFs [34] as

$$\underbrace{\begin{pmatrix} \mathbf{B}_1 & \mathbf{B}_2 & \dots & \mathbf{B}_K \end{pmatrix}}_{\mathbf{B}} \underbrace{\begin{pmatrix} \mathbf{t}_1 & \mathbf{t}_2 & \dots & \mathbf{t}_K \end{pmatrix}^T}_{\mathbf{t}} = \begin{pmatrix} \mathbf{z}_d \end{pmatrix}, \tag{7}$$

where K is the number of TIFs and $\mathbf{B}_i$ is the convolution matrix for the ith TIF. This non-sequential optimization considers all the TIFs at the same time, which can potentially reduce the MSF errors. It has even been demonstrated that multiple TIFs can be multiplexed in a single run to further improve the polishing efficiency [38], if the dwell time of each TIF is well optimized and their total dwell time is balanced (*i.e.,* close to each other). However, the existing method does not guarantee the positiveness and smoothness of the dwell time, and the dwell time balance of each TIF is not considered, which restricts its wider application in real CCOS processes.

To solve these problems, the STO method introduced in Section 3 is extended, and an innovative concurrent Multi-Tool Optimization (MTO) algorithm shown in Algorithm 2 is proposed, where

one λ is utilized to optimize the dwell time for multiple TIFs as

$$
\left(\underbrace{\begin{matrix} \mathbf{B}_1 & \mathbf{B}_2 & \ldots & \mathbf{B}_K \end{matrix}}_{\substack{\mathbf{B} \\ \lambda\mathbf{I}}} \right) \underbrace{\begin{pmatrix} \mathbf{t}_1 & \mathbf{t}_2 & \ldots & \mathbf{t}_K \end{pmatrix}^T}_{\mathbf{t}} = \begin{pmatrix} \mathbf{z}_d \\ \mathbf{0} \end{pmatrix},
\tag{8}
$$

in which case, an implicit regularization is automatically added to MTO to balance the dwell time solutions among different TIFs. Another two differences between MTO and STO are highlighted in Algorithm 2. On one hand, as shown in Line 2, the minimum dwell time, τ_i, is calculated for the ith TIF, depending on its own tool-path intervals. On the other hand, the positiveness adjustment, as shown in Lines 21 - 27, is performed for each TIF individually using its own τ_i.

The simulation with MTO is shown in Fig. 5(b). Compared with the STO result in Fig. 5(a), the dwell time for each TIF is closer to each other, and the total dwell time of MTO (*i.e.,* 70.70 + 85.02 + 335.44 = 491.16 min) is much shorter than that of STO (*i.e.,* 96.58 + 284.97 + 2,412.78 = 2,794.33 min). Furthermore, from the center profiles along the *x*-direction shown in Fig. 5(c), MTO achieves much smoother dwell time solutions. It is also worth emphasising that these MTO results are obtained without performing the surface extension, which is the necessary step for STO as mentioned in Section 3.2.3. Although the final residual RMS estimated by MTO is slightly larger than that by STO, this estimation is more reasonable and easier to implement in practice, which will be verified by a real experiment in Section 5.

5. Experiment

To verify the practical applicability of the proposed MTO method, as shown in Fig. 6, a polishing experiment is performed on a Zeeko IRP200 7-axis CNC polishing machine. Three bonnet tools with the radii of 42.90 mm, 21.99 mm, and 11.54 mm are used in this experiment. The tool footprints are obtained by dwelling each tool at one spot for a certain amount of time, from which the TIFs are extracted, which have the sizes of 12 mm, 8 mm, and 5 mm, respectively, and the Peak Removal Rates (PRRs) of 327.5 nm/s, 114.8 nm/s, and 97.6 nm/s, respectively.
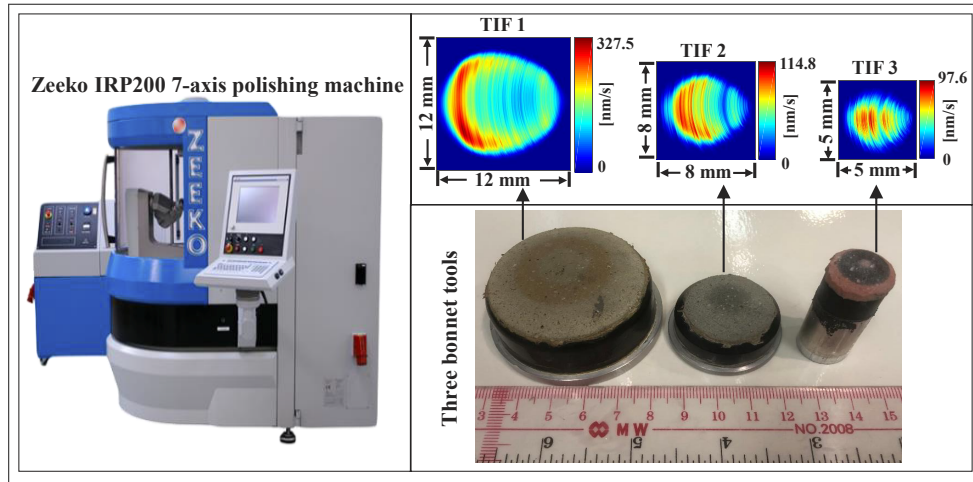

Fig. 6. The experiment is performed on a Zeeko IRP200. Three bonnet tools with the radii of the curvature of 42.90 mm, 21.99 mm, and 11.54 mm are used. The corresponding TIF sizes are 12 mm, 10 mm, and 5 mm, respectively.

The workpiece, as shown in Fig. 7(a), is a 100 mm × 100 m HK9L glass mirror. The center 60 mm × 60 mm is defined as the CA that needs to be polished. The target removal in the CA, as shown in Fig. 7(b), is measured by a Zygo interferometer, and the initial surface error is 45.42 nm RMS.
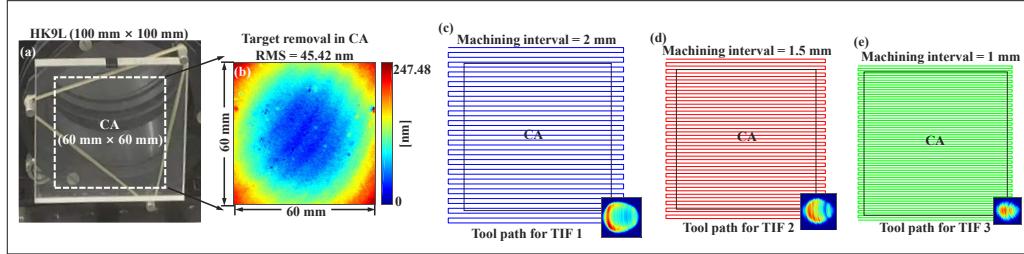

Fig. 7. The HK9L mirror is measured with a Zygo interferometer (a), and the target removal in the center 60 mm × 60 mm CA (b) will be removed by the three TIFs using the raster tool paths with the machine intervals of 2 mm (c), 1.5 mm (d), and 1 mm (e), respectively.

The raster tool paths scanning along the *y* direction, as shown in Figs. 7(c),7(d) and 7(e), are used for all three tools. To minimize the possible middle-frequency errors generated by the tool footprints, the distance between each two consecutive dwell points and the scanning interval in the *y* direction are both set based on the criterion [39] as

$$\Delta x = \frac{\pi \cdot d}{18}, \tag{9}$$

where *d* is the diameter of a TIF. Therefore, the machining intervals for the three tools are determined as 2.10 mm, 1.40 mm and 0.87 mm, respectively, which are clamped to 2 mm, 1.5 mm and 1 mm, respectively, for simplicity. Also, to avoid the edge effect (which is not considered in this study), the range of the dwell points is set to be larger than the outline perimeter of the CA by the radius of the used TIF.

5.1. STO vs. MTO

The performances of the STO and MTO are studied on the measured surface and TIFs before implementing the experiment. In the sequential process, the single-tool strategies are applied sequentially to calculate the dwell time for each TIF individually. The optimization of the current TIF is based on the estimated residual error from the last TIF. In the MTO process, the multi-tool method proposed in Section 4 is used. The STO and MTO calculated dwell time for the three TIFs and the estimated residual error maps are shown in Figs. 8(a) and 8(b), respectively.

It is found that the estimated residuals in the CA optimized by the STO and MTO methods are similar, with only 0.4 nm RMS difference. However, STO costs longer total dwell time than MTO Specifically, the additional time is brought by TIF 3 in the sequential result. This is because, as shown in Fig. 8(a), the dwell time for TIF 2 is so close to each other, which indicates that it cannot effectively correct the residual errors left by TIF 1. Therefore, TIF 3 requires more time to converge. On the other hand, as shown in Fig. 8(b), the dwell time obtained from MTO is more balanced. Each TIF removes a portion of the target removal map in the CA shown in Fig. 7(b), but the combination of the three converge to the same residual. In addition, the center profiles of the dwell time maps are compared in Fig. 8(c). The dwell time profiles for TIF 1 optimized from both STO and MTO are similar, since they are calculated based on the same target removal map. The profiles for TIF 2 and TIF 3 are very different from each other. Especially, for TIF 3, the MTO calculated dwell time profile is much smoother than the sequentially optimized one, and thus will exert less stress on the CNC dynamics. Based on these analyses, the MTO calculated
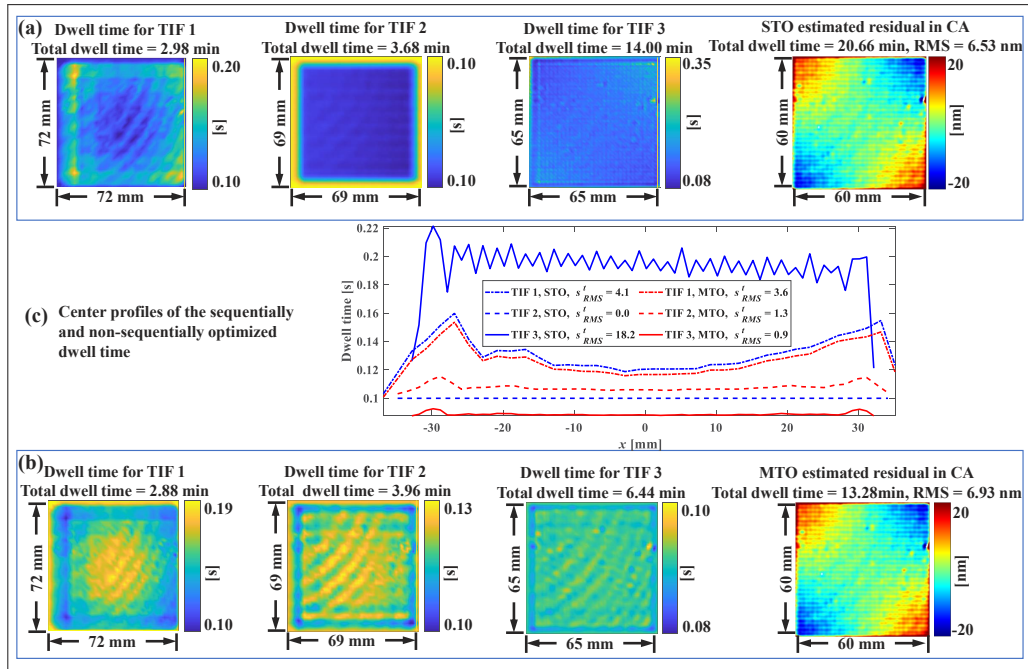
Fig. 8. Comparison between the STO (a) and the MTO (b) optimized dwell time for the three TIFs. The center profiles of the dwell time maps (c) and the total run time prove the superiority of MTO, which enables both robust and efficient CCOS process optimization.

dwell time for the three tools shown in Fig. 8(b) is thus selected to guide the real experiment that will be illustrated in the next subsection.

5.2. Experiment result of MTO

The experiment result using MTO is shown in Fig. 9. The three bonnet tools are used in turn, and the final residual error in the CA reaches 11.18 nm RMS, which is slightly larger than the estimation given in Fig. 8(b), yet the shapes of both the measured and estimated residual maps in the CA are very similar to each other.
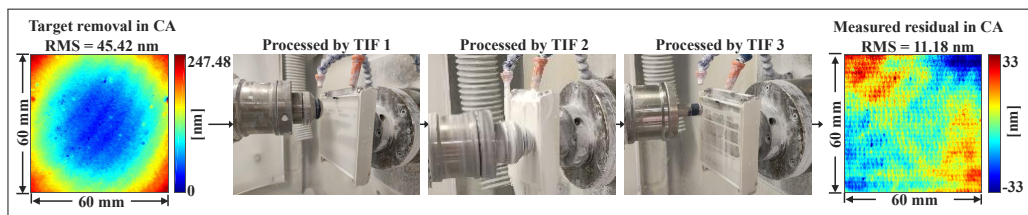

Fig. 9. Experiment result using the MTO for the three tools. The measured 11.18 nm RMS residual error in the CA is close to the estimated 6.93 nm RMS.

The discrepancy between the real experiment and estimation is resulted from two issues. Firstly, the TIFs used in the experiment are so powerful (97.6 nm/s - 327.5 nm/s PRR) but the target removal is so small (45.42 nm RMS) that the CNC dynamics can hardly match the rapid motion requirement. This introduces a constant extra time to each segment on one tool path, which influences the convergence of the real polishing process. It is worth mentioning that

an estimated residual of 2.1 nm RMS can be achieved with the proposed MTO method if the maximum feedrate constraint is removed. The actual residual after the polishing experiment can thus be expected to be at least lower than 5 nm RMS. In addition, certain waviness features are found in the measured residual map in the CA as shown in Fig. 9. Either a smoothing or a polishing process with a smaller tool is necessary to remove these features, if an application requires tighter mid-to-high spatial frequency specifications (*e.g.,* Power Spectral Density or Structure Function).

6. Discussion

It is worth mentioning that, as shown in Figs. 8(a) and 8(b), the final residual optimized by MTO is slightly larger than that optimized by STO, which is due to the same damping factor, λ, used for regularization of the three tools. If further improvement of the residual is expected, multiple MTO iterations can be carried out by gradually reducing the number of Tool Influence Functions (TIFs). Figure 10 gives an example of a 3-iteration MTO on the simulation data shown in Fig. 1. In the first iteration, three TIFs are used. Afterwards, TIF 1 is removed from the second iteration, and only TIF 3 is used in the last iteration. After each iteration, the dwell time for the corresponding tool is accumulated. It can be found that the final residual is reduced to the same level as the STO result shown in Fig. 8(a) while the total dwell time for TIF 3 is greatly increased, which indicates that the surface error contains certain high-frequency components that only the smallest TIF 3 is capable of correcting them.
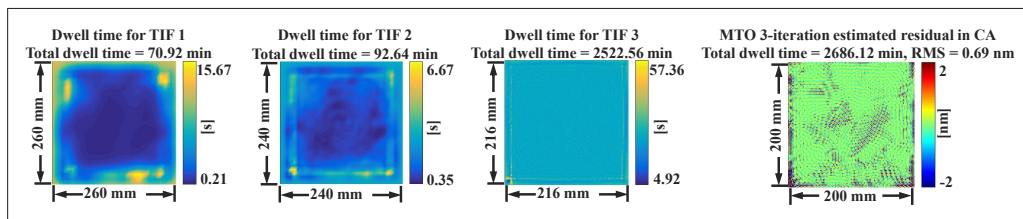

Fig. 10. Three iterations of MTO applied to calculate the dwell time for the three TIFs.

Even though the estimated accuracy obtained from the iterative MTO shown in Fig. 10 is higher, it is not recommended to use this solution in practice, especially when the three TIFs will be multiplexed in a single run in a real CCOS process [38], which requires the total dwell time of each tool to be balanced. We are currently working on an optimization method dedicated to multi-tool multiplexing CCOS processes and will report the progress in the near future.

7. Concluding remarks

In this paper, a systematic study for multi-tool dwell time optimization was conducted. Firstly, LSMR was selected as the solver for the matrix-based dwell time algorithm for its faster convergence. The key parameters, including the maximum number of iterations and the damping factor, are then evaluated. Secondly, based on LSMR, the Single-Tool Optimization (STO) method was proposed, which was able to obtain a positive and smooth dwell time solution while considering the CNC dynamics limit and keeping a low estimated residual in the clear aperture. Thirdly, STO was extended, and an improved, Multi-Tool Optimization (MTO) method was proposed that further balanced the dwell time among different tools. Finally, the advantages of the proposed MTO have been verified with both a simulation and an experiment, which demonstrated its effectiveness and practical applicability in multi-tool Computer-Controlled Optical Surfacing (CCOS) applications. MTO can also be applied to the fabrication of large-aperture optics, such as

the base mirrors for the telescopes and the optical components in high-power laser systems, where the improvement of efficiency means a great reduction in manpower and financial investments.

Disclosures. The authors declare no conflicts of interest.

Data availability. Data underlying the results presented in this paper are not publicly available at this time but may be obtained from the authors upon reasonable request.

References

1. L. R. Graves, G. A. Smith, D. Apai, and D. W. Kim, "Precision optics manufacturing and control for next-generation large telescopes," Nanomanuf. Metrol. **2**(2), 65–90 (2019).
2. J. Fanson, R. Bernstein, G. Angeli, D. Ashby, B. Bigelow, G. Brossus, A. Bouchez, W. Burgett, A. Contos, R. Demers, F. Figueroa, B. Fischer, F. Groark, R. Laskin, R. Millan-Gabet, M. Pi, and N. Wheeler, "Overview and status of the giant magellan telescope project," in *Ground-based and Airborne Telescopes VIII*, vol. 11445 (International Society for Optics and Photonics, 2020), p. 114451F.
3. A. Beaucamp and Y. Namba, "Super-smooth finishing of diamond turned hard x-ray molding dies by combined fluid jet and bonnet polishing," CIRP Ann. **62**(1), 315–318 (2013).
4. H. Thiess, H. Lasser, and F. Siewert, "Fabrication of x-ray mirrors for synchrotron applications," Nucl. Instrum. Methods Phys. Res., Sect. A **616**(2-3), 157–161 (2010).
5. L. Wischmeier, P. Graeupner, P. Kuerz, W. Kaiser, J. van Schoot, J. Mallmann, J. de Pee, and J. Stoeldraijer, "High-NA EUV lithography optics becomes reality," in *Extreme Ultraviolet (EUV) Lithography XI*, vol. 11323 (International Society for Optics and Photonics, 2020), p. 1132308.
6. R. A. Jones, "Optimization of computer controlled polishing," Appl. Opt. **16**(1), 218–224 (1977).
7. D. D. Walker, D. Brooks, A. King, R. Freeman, R. Morton, G. McCavana, and S.-W. Kim, "The 'precessions' tooling for polishing and figuring flat, spherical and aspheric surfaces," Opt. Express **11**(8), 958–964 (2003).
8. C. Wang, C. F. Cheung, L. Ho, M. Liu, and W. B. Lee, "A novel multi-jet polishing process and tool for high-efficiency polishing," Int. J. Mach. Tools Manuf. **115**, 60–73 (2017).
9. H. Kansal, A. K. Singh, and V. Grover, "Magnetorheological nano-finishing of diamagnetic material using permanent magnets tool," Precis. Eng. **51**, 30–39 (2018).
10. T. Wang, L. Huang, M. Vescovi, D. Kuhne, Y. Zhu, V. S. Negi, Z. Zhang, C. Wang, X. Ke, H. Choi, W. P. Pullen, D. Kim, Q. Kemao, K. Nakhoda, N. Bouet, and M. Idir, "Universal dwell time optimization for deterministic optics fabrication," Opt. Express **29**(23), 38737–38757 (2021).
11. L. Zhou, Y.-f. Dai, X.-h. Xie, C.-j. Jiao, and S.-y. Li, "Model and method to determine dwell time in ion beam figuring," Nanotechnol. Precis. Eng. **5**, 107–112 (2007).
12. Y. Mizoue, B. Sencer, and A. Beaucamp, "Identification and optimization of cnc dynamics in time-dependent machining processes and its validation to fluid jet polishing," Int. J. Mach. Tools Manuf. **159**, 103648 (2020).
13. P. Van Cittert, "Zum einfluss der spaltbreite auf die intensitätsverteilung in spektrallinien. ii," Z. Phys. **69**(5-6), 298–308 (1931).
14. C. Wang, W. Yang, Z. Wang, X. Yang, C. Hu, B. Zhong, Y. Guo, and Q. Xu, "Dwell-time algorithm for polishing large optics," Appl. Opt. **53**(21), 4752–4760 (2014).
15. N. Hill and G. Ioup, "Convergence of the van cittert iterative method of deconvolution," J. Opt. Soc. Am. **66**(5), 487–489 (1976).
16. S. Wilson and J. McNeil, "Neutral ion beam figuring of large optical surfaces," in *Current developments in optical engineering II*, vol. 818 (International Society for Optics and Photonics, 1987), pp. 320–324.
17. T. Wang, L. Huang, H. Kang, H. Choi, D. W. Kim, K. Tayabaly, and M. Idir, "RIFTA: A robust iterative fourier transform-based dwell time algorithm for ultra-precision ion beam figuring of synchrotron mirrors," Sci. Rep. **10**(1), 8135 (2020).
18. T. Wang, L. Huang, H. Choi, M. Vescovi, D. Kuhne, Y. Zhu, W. C. Pullen, X. Ke, D. W. Kim, Q. Kemao, K. Tayabaly, N. Bouet, and M. Idir, "RISE: robust iterative surface extension for sub-nanometer x-ray mirror fabrication," Opt. Express **29**(10), 15114–15132 (2021).
19. L. B. Lucy, "An iterative technique for the rectification of observed distributions," The astronomical journal **79**, 745 (1974).
20. W. H. Richardson, "Bayesian-based iterative method of image restoration," J. Opt. Soc. Am. **62**(1), 55–59 (1972).
21. C. Jiao, S. Li, and X. Xie, "Algorithm for ion beam figuring of low-gradient mirrors," Appl. Opt. **48**(21), 4090–4096 (2009).
22. C. L. Carnal, C. M. Egert, and K. W. Hylton, "Advanced matrix-based algorithm for ion-beam milling of optical components," in *Current Developments in Optical Design and Optical Engineering II*, vol. 1752 (International Society for Optics and Photonics, 1992), pp. 54–62.
23. J. F. Wu, Z. W. Lu, H. X. Zhang, and T. S. Wang, "Dwell time algorithm in ion beam figuring," Appl. Opt. **48**(20), 3930–3937 (2009).

24. Z. Dong, H. Cheng, and H.-Y. Tam, "Robust linear equation dwell time model compatible with large scale discrete surface error matrix," Appl. Opt. **54**(10), 2747–2756 (2015).
25. Z. Dong and H. Cheng, "Toward the complete practicability for the linear-equation dwell time model in subaperture polishing," Appl. Opt. **54**(30), 8884–8890 (2015).
26. C. Song, Y. Dai, and X. Peng, "Model and algorithm based on accurate realization of dwell time in magnetorheological finishing," Appl. Opt. **49**(19), 3676–3683 (2010).
27. L. Li, D. Xue, W. Deng, X. Wang, Y. Bai, F. Zhang, and X. Zhang, "Positive dwell time algorithm with minimum equal extra material removal in deterministic optical surfacing technology," Appl. Opt. **56**(32), 9098–9104 (2017).
28. T. Wang, L. Huang, M. Vescovi, D. Kuhne, K. Tayabaly, N. Bouet, and M. Idir, "Study on an effective one-dimensional ion-beam figuring method," Opt. Express **27**(11), 15368–15381 (2019).
29. W. Zhu and A. Beaucamp, "Zernike mapping of optimum dwell time in deterministic fabrication of freeform optics," Opt. Express **27**(20), 28692–28706 (2019).
30. Y. Zhang, F. Fang, W. Huang, and W. Fan, "Dwell time algorithm based on bounded constrained least squares under dynamic performance constraints of machine tool in deterministic optical finishing," Int. J. Precis. Eng. Manuf. Technol. **8**(5), 1415–1427 (2021).
31. C. C. Paige and M. A. Saunders, "LSQR: An algorithm for sparse linear equations and sparse least squares," ACM Transactions on Math. Softw. (TOMS) **8**(1), 43–71 (1982).
32. Y. Han, F. Duan, W. Zhu, L. Zhang, and A. Beaucamp, "Analytical and stochastic modeling of surface topography in time-dependent sub-aperture processing," Int. J. Mech. Sci. **175**, 105575 (2020).
33. Y. Han, W.-L. Zhu, L. Zhang, and A. Beaucamp, "Region adaptive scheduling for time-dependent processes with optimal use of machine dynamics," Int. J. Mach. Tools Manuf. **156**, 103589 (2020).
34. D. W. Kim, S.-W. Kim, and J. H. Burge, "Non-sequential optimization technique for a computer controlled optical surfacing process using multiple tool influence functions," Opt. Express **17**(24), 21850–21866 (2009).
35. D. C.-L. Fong and M. Saunders, "LSMR: An iterative algorithm for sparse least-squares problems," SIAM J. Sci. Comput. **33**(5), 2950–2971 (2011).
36. C. Audet and J. E. Dennis Jr, "Analysis of generalized pattern searches," SIAM J. Optim. **13**(3), 889–903 (2002).
37. Z. Dong, H. Cheng, and H.-Y. Tam, "Modified dwell time optimization model and its applications in subaperture polishing," Appl. Opt. **53**(15), 3213–3224 (2014).
38. X. Ke, T. Wang, H. Choi, W. Pullen, L. Huang, M. Idir, and D. W. Kim, "Dual-tool multiplexing model of parallel computer controlled optical surfacing," Opt. Lett. **45**(23), 6426–6429 (2020).
39. X. Xie and S. Li, *Ion Beam Figuring Technology* (Springer, 2015), pp. 1343–1390.